1   A computational model of shared fine-scale structure in the human connectome

2   Short title: Common model of the human connectome

3   J. Swaroop Guntupalli[1,2,3], Ma Feilong[1,2], James V. Haxby[1,2,*]

4   [1]Department of Psychological and Brain Sciences, Dartmouth College, Hanover, NH,

5   03755 USA

6   [2]Center for Cognitive Neuroscience, Dartmouth College, Hanover, NH 03755 USA

7   [3]Vicarious AI, Union City, CA USA

8   *Correspondence to: james.v.haxby@dartmouth.edu

9

Abstract

10   Variation in cortical connectivity profiles is typically modeled as having a coarse spatial

11   scale parcellated into interconnected brain areas. We created a high-dimensional

12   common model of the human connectome to search for fine-scale structure that is

13   shared across brains. Projecting individual connectivity data into this new common

14   model connectome accounts for substantially more variance in the human connectome

15   than do previous models. This newly discovered shared structure is closely related to

16   fine-scale distinctions in representations of information. These results reveal a shared

17   fine-scale structure that is a major component of the human connectome that coexists

18   with coarse-scale, areal structure. This shared fine-scale structure was not captured in

19   previous models and was, therefore, inaccessible to analysis and study.

20

Author Summary

21

Resting state fMRI has become a ubiquitous tool for measuring connectivity in normal and diseased brains. Current dominant models of connectivity are based on coarse-scale connectivity among brain regions, ignoring fine-scale structure within those regions. We developed a high-dimensional common model of the human connectome that captures both coarse and fine-scale structure of connectivity shared across brains. We showed that this shared fine-scale structure is related to fine-scale distinctions in representation of information, and our model accounts for substantially more shared variance of connectivity compared to previous models. Our model opens new territory — shared fine-scale structure, a dominant but mostly unexplored component of the human connectome — for analysis and study.

31   Introduction

32   Resting state functional magnetic resonance imaging (rsfMRI) reveals patterns of

33   functional connectivity that are used to investigate the human connectome [1-3] and

34   parcellate the brain into interconnected areas that form brain systems and can be

35   modeled as networks [4-11]. The connectivity of a single area is considered to be

36   relatively homogeneous and typically is modeled as a mean connectivity profile.

37   Cortical topography, however, has both a coarse scale of cortical areas and a finer scale

38   of multiplexed topographies within areas [12-16]. Fine-scale within-area topographies

39   are reflected in patterns of activity that can be measured with fMRI and decoded using

40   multivariate pattern analysis (MVPA)[12,13,17]. Fine-scale variation in connectivity,

41   however, has been overlooked due to poor anatomical alignment of this variation

42   across individual brains. We ask here whether local variation in functional connectivity

43   also has a fine-scale structure, similar to fine-scale response tuning topographies, and

44   whether such variation can be captured in a common model with basis functions that

45   are shared across brains.

46   We developed a new algorithm, connectivity hyperalignment (CHA), to model

47   local variation in connectivity profiles with shared basis functions for connectivity

48   profiles across individuals and individual-specific local topographies of those

49   connectivity basis functions (Fig 1). The resultant common model connectome consists

50   of transformation matrices for each individual brain, which contain individual-specific

51   topographic basis functions, and a common model connectome space, which contains

52   shared connectivity profiles (Fig 2). Individual transformation matrices transform an

53   individual brain's connectome, in its native anatomical coordinate space, into the

54   common model space [13,16]. The individual transformation matrices and common

55   model connectivity matrix are derived iteratively from training data. Validity testing is

56   done on connectivity profiles and other functional parameters from independent test

57   data that are hyperaligned into the common model connectome space. The results

58   show that CHA can derive these shared basis functions from functional connectivity

59   derived from neural activity while watching an audiovisual movie and from neural

60   activity in the resting state.

61

Fig 1. Schematic of connectivity hyperalignment (CHA).

(A) Connectivity can be defined as any measure of similarity between a cortical locus (e.g., surface node/voxel) and a target region. Connectivities to a target region (T_i, T_j, T_k, ...) of loci in a searchlight yield a connectivity pattern for that target in that searchlight. These patterns can be analyzed as connectivity pattern vectors (V_i, V_j, V_k, ...) in a space in which each cortical locus in that region is a dimension. (B) Connectivity pattern vectors (V_1, V_2, ... V_n) in a region of interest or a searchlight to be hyperaligned are calculated for target regions (T_1, T_2..., T_n,) distributed uniformly across the whole cortex. At this stage connectivity hyperalignment derives transformation matrices for each brain (R_1, R_2, ...) in each searchlight that align these vectors across subjects into a common high-dimensional connectivity space. (C) For each subject, searchlight transformation matrices are aggregated into a whole cortex transformation matrix, R_{1A}, as in [16], affording projection of connectivity data into a whole cortex common model connectome space. Conversely, the transpose of a whole cortex transformation matrix can project connectivity data from the whole cortex common connectome space back into that subject's cortical anatomy.

75   Figure 2. Schematic of data and transformation matrices for the common connectome.

76   The connectivity data for an individual subject, i, in that subject's native brain space, B_i, is projected

77   into the common model connectome space, M_i, by multiplying it with the transformation matrix, R_i.

78   Vectors in data matrix rows are connectivity pattern vectors — patterns of connectivity with a single

79   connectivity target time-series across cortical nodes/voxels in the individual's native brain space or

80   across model dimensions in the common model connectome. Vectors in data matrix columns are

81   connectivity profile vectors — connectivities of a single node/voxel or model dimension across

82   connectivity targets. The transformation matrix contains weights for the linear transformation of

83   connectivity vectors in an individual's brain data space into the common model connectome space.

84   Vectors in transformation matrix columns for model dimensions are patterns of weights for a local

85   field of voxels/nodes and serve as topographic basis functions. Individual variation in the fine-scale

86   topographic pattern of connectivity to a target is modeled as a weighted mixture of multiplexed or

87   overlaid topographies for model dimensions.

88   The resultant common model connectome accounts for substantially more

89   shared variance in functional connectivity derived from both movie fMRI data and

90   resting state fMRI data than was accounted for by previous models. This shared

91   variance resides in fine-scale local variations in connectivity. We show further that this

92   local variability in functional connectivity profiles is meaningful in that it is closely

93   related to local patterns of response that encode fine distinctions among

94   representations. Our results indicate that shared fine-scale local variation, which was

95   not evident in previous models, is a major component of the human connectome that

96   coexists with shared coarse-scale areal structure. Our common model connectome

97   makes this fine-scale local variation accessible for group-level study of its network

98   properties.

99   ## Results

100   We derived a common model of the human connectome by applying CHA to

101   fMRI data collected while 11 subjects viewed a full-length movie [13,16] and to rsfMRI

102   data for 20 subjects in the Human Connectome Project (HCP) database [18-20]. The

103   common model connectome is high-dimensional with connectivity profiles for model

104   dimensions that serve as basis functions for modeling the connectivity profiles of

105   cortical loci in individual brains. We validated the common model in terms of 1)

106   increased intersubject correlations (ISCs) of connectivity profiles, and 2) increased

107   spatial specificity of shared connectivity profiles. To test whether this fine-scale

108   structure is meaningful for the representation of information, we tested the effect of

109   CHA on 3) ISCs of representational geometry for the movie, 4) between-subject

110   multivariate pattern classification (bsMVPC) of responses to the movie and 5) ISCs of

111   task activation and contrast maps from the HCP database. The first two validation

112   experiments are designed to test whether connectivity hyperalignment improves

113   alignment of functional connectivity across brains in a way that preserves the fine-grain

114   spatial granularity of variation in connectivity profiles. These validations were tested on

115   functional connectivity derived from both the movie and rsfMRI data. The third, fourth,

116   and fifth validation experiments are designed to test whether the transformation of

117   individual brain spaces into the common model space better aligns topographies

118   associated with representation of information and cognitive processes. The third and

119   fourth validations were tested on the movie data. The fifth validation test used rsfMRI

120   and task fMRI data from the HCP database.

121   *Intersubject correlation of connectivity profiles*

122   CHA afforded large increases in ISCs of connectivity profile vectors in both the

123   movie fMRI data and the rsfMRI data (Figures 3 and 4).

124   Increases in ISCs of functional connectivity derived from movie data were

125   distributed across all of cortex (Fig 3). ISC at a cortical node is the correlation of the

126   one subject's connectivity profile with the mean of other subjects' profiles, indexing

127   how well other subjects' connectivity profiles can predict an individual's connectivity

128   profiles. Fig 3A shows a cortical map of mean ISCs of connectivity profiles in the

129   common model connectome space as compared to ISCs in anatomically-aligned data.

130   Fig 3B is a scatterplot of mean ISCs for individuals after anatomical alignment and

131   CHA, which shows that CHA increased ISC for each individual and preserved individual

132   similarity or deviance from the group. We quantify the increases in 24 functional ROIs,

133   identified using a meta-analytic database, NeuroSynth [21](Fig 3C; table S1). Mean ISC

134   of connectivity profiles across these ROIs was markedly higher in the common model

135   connectome than in the anatomically-aligned data (0.67 versus 0.15; difference = 0.52,

136   95% confidence interval, CI = [0.46, 0.56]).

137
         Fig 3. ISC of connectivity profiles calculated from movie data. (A) Average ISCs of connectivity

138   profiles in each surface node after CHA and anatomical alignment. (B) Scatter plot of individual

139   whole cortex mean ISCs of connectivity profiles before and after CHA with linear fit. Each

140   subject's similarity of connectome with the group is improved by CHA while preserving similarity

141   or deviance from others. Shaded region is the 95% CI. (C) Mean ISCs of connectivity profiles in

142   functional ROIs covering visual, auditory, cognitive, and social systems comparing the common

143   model connectome space and anatomical alignment. Bootstrapped testing showed significantly

144   higher ISCs after CHA than after anatomical alignment in all ROIs.

145   Increases in ISCs of resting state connectivity profiles were similarly distributed

146   across all of cortex and replicated the findings based on ISCs of movie viewing

147   connectivity profiles (Fig 4). Fig 4A shows a cortical map of mean ISCs of resting state

148   connectivity profiles in the common model connectome space and in data aligned with

149   the HCP's MSM-All method (multimodal surface matching [22]). Fig 4B is a scatterplot

150   of mean ISCs for individuals after MSM-All alignment and CHA, which shows that CHA

151   of resting state data increased ISC for each individual and preserved individual

152   similarity or deviance from the group. Fig 4C shows a cortical map of within-subject

153   correlations between connectivity profiles from different resting state sessions. We

154   quantify the increases in 26 functional ROIs, identified using a meta-analytic database,

155   NeuroSynth [21](Fig 4D; table S1). Mean ISC of connectivity profiles across these ROIs

156   was markedly higher in the common model connectome than in the MSM-All-aligned

157   data (0.66 versus 0.35; difference = 0.31 [0.30, 0.33]). ISCs of resting state connectivity

158   profiles in the common model connectome space are slightly higher than

159   within-subject correlations of resting state connectivity profiles (mean correlation =

160   0.64; CI for difference = [0.00, 0.05]) (Fig 4D). This latter result indicates that an

161   individual's connectome based on resting state functional connectivity is better

162   predicted by the common model connectome, based on other subjects' data, than by

163   estimates based on a typical sample of that subject's own rsfMRI data, due to the

164   benefit of estimating connectivity profiles based on a large number of brains and the

165   precision of CHA.

166

Fig 4. ISC of connectivity profiles calculated from HCP rsfMRI data. (A) Average ISC of

167   connectivity profiles in each surface node in the common model connectome space and after

168   surface alignment (MSM-All). (B) Scatter plot of individual whole cortex mean ISCs of connectivity

169   profiles before and after CHA with linear fit. Each subject's similarity of connectome with the

170   group is improved by CHA while preserving similarity or deviance from others. Shaded region is

171   the 95% CI. (C) Average within-subject between-session correlations in the common space. (D)

172   Mean ISCs and WSCs of connectivity profiles in functional ROIs covering visual, auditory,

173   cognitive, and social systems comparing the common model connectome space, within-subject

174   between-session correlation in common space, and surface alignment.

175   The substantial increase in ISCs with hyperalignment is due in part to discovery

176 of shared variance that was obscured by misalignment but also to suppression of

177 unshared variance and amplification of shared variance mediated by filtering the data

178 in the transformation step with smaller weights for nodes with unshared or noisy

179 variance and larger weights for nodes with shared variance. To gauge the size of the

180 effect of filtering independent of better information alignment, we calculated ISCs in

181 data that are filtered by our algorithm but aligned based on anatomy or MSM-All (see

182 methods).   ROI mean ISCs of connectivity profiles in movie data filtered with CHA but

183 aligned based on anatomy was 0.22 (CHA versus filter-control difference = 0.45 [0.39

184 0.49]) and for HCP resting state data filtered with CHA but aligned based on MSM-All

185 was 0.41 (CHA versus filter-control difference = 0.25 [0.23, 0.27]). These ISCs are larger

186 than ISCs of unfiltered, anatomically and MSM-All-aligned data but, nonetheless, still

187 markedly lower than ISCs of connectivity profiles in the common model connectome

188 space, which is both filtered and re-aligned by CHA.

189　　*Spatial granularity of connectivity profile variation*

190　　　　We investigated the spatial specificity of the common model connectome by

191　　computing the intersubject spatial point spread functions (PSF) of ISCs of connectivity

192　　profiles [16]. The PSF of connectivity profiles was computed as the correlation of the

193　　connectivity profile in a cortical surface node for a given subject with the average

194　　connectivity profiles of other subjects in the same node and nodes at cortical distances

195　　ranging from 3 to 12 mm. We similarly calculated within-subject PSFs based on

196　　within-subject correlations (WSC) of connectivity profiles between two resting state

197　　sessions. Fig 5A shows the slopes of connectivity profile PSFs for movie data in 24

198　　functionally-defined ROIs , and Fig 5B shows the mean PSF across these ROIs as a

199　　function of cortical distance) in the common model connectome space and in

200　　anatomically-aligned data. CHA increased the average slope of PSF across these ROIs,

201　　relative to anatomical alignment, from 0.013 to 0.105 (difference=0.092 [0.080, 0.099]).

202　　Fig 5C shows the slopes of connectivity profile PSFs for resting state connectivity

203　　profiles in the 26 functionally-defined ROIs, and Fig 5D shows the mean PSF across

204　　these ROIs (ISC or WSC as a function of cortical distance) in the common model

205　　connectome space, in MSM-All-aligned data, and within-subject. CHA increased the

206　　average slope of PSF across these ROIs, relative to MSM-All alignment, from 0.012 to

207　　0.065 (difference=0.053 [0.047, 0.055]). The intersubject PSF slopes in the common

208　　model connectome space and the PSF within-subject (slope = 0.067) were not

209　　significantly different (difference = 0.002 [-0.002, 0.007]). This fine spatial granularity

210　　was ubiquitous in cortex, with steep PSFs in sensory-perceptual areas in occipital and

211   temporal cortices as well as in higher-order cognitive areas in lateral and medial

212   parietal and prefrontal cortices.

213   Fig 5. Spatial granularity of shared connectivity profiles. The intersubject point spread function

214   (PSF) of connectivity profile correlations are computed as the correlation between the

215   connectivity profile for a cortical locus in one subject and the profiles of the same locus and its

216   spatial neighbors in other subjects at increasing distances from that locus. For the HCP rsfMRI

217   data, within-subject PSFs are computed as the correlation between the connectivity profile for a

218   cortical locus from one rsfMRI session and the profiles of the same locus and its spatial neighbors

219   from a different rsfMRI session. Slope is estimated in each functional ROI as the linear fit of

220   intersubject or within subject correlations as a function of distance. (A) Slope of PSFs for movie

221   viewing connectivity profiles in 24 functional ROIs. (B) Average movie viewing connectivity PSF

222   across all ROIs is plotted as ISC as a function of cortical distance. (C) Slope of PSFs for resting

223   state connectivity profiles in 26 functional ROIs. (D) Average resting state connectivity PSF

224   across all ROIs is plotted as ISC or WSC as a function of cortical distance.

225   The mean PSFs across ROIs (Fig 5B and 5D), clearly show that CHA captures

226   fine-scale variations in connectivity profiles for neighboring cortical nodes across

227   subjects that are not captured by anatomical alignment or MSM-All alignment. The

228   ISCs of connectivity profiles for neighboring nodes in the common model connectome

229   are substantially lower than ISCs for the same node (movie data: 0.21 [0.18, 0.23];

230   resting state: 0.09 [0.08,0.09]). Similar fine spatial granularity is seen in the

231   within-subject between-session PSFs for resting state connectivity profiles (0.10 [0.09,

232   0.10]). By contrast, ISCs for connectivity profiles in the anatomically-aligned and

233   MSM-All aligned data barely differ for nodes spaced 0 versus 1 voxel/3 mm (differences

234   =0.005, [0.005, 0.005] and 0.004, [0.004,0.015], respectively) and 2 voxels/6 mm (0.01

235   [0.01, 0.02] and 0.02 [0.01, 0.02], respectively) apart. Decrements for larger distances

236   (ISCs of nodes spaced 3 voxels/9 mm: 0.03 [0.03, 0.03] and 0.03 [0.03,0.03],

237   respectively; and 4 voxels/12 mm: (0.05 [0.05, 0.06] and 0.05 [0.04,0.05], respectively)

238   were similarly small.

239
Generalization to fine-scale patterns in response tuning

240   Next we asked if this shared variance in fine-scale local variation in connectivity

241   profiles carries meaning by testing whether it reflects fine-scale variations in response

242   tuning topographies that carry fine-grained distinctions in representation. We tested

243   whether projecting movie response data into the CHA-derived common connectome

244   space afforded better alignment of representational geometry for movie time-points

245   and better bsMVPC of movie time segments.

246   Results show that shared fine-scale structure in the common model connectome

247   is closely related to fine distinctions in representations. Fig 6A shows a cortical map of

248   mean ISCs of local representational geometry after anatomical alignment and in the

249   common model connectome. Representational geometry is the matrix of all pairwise

250   similarities between patterns of response to different time-points in the movie, resulting

251   in a matrix of more than 800,000 pairwise similarities (see methods). Fig 6B shows a

252   cortical map of mean bsMVPC accuracies for 15 s movie time-segments in searchlights

253   after anatomical alignment and CHA. CHA greatly increased both ISCs of

254   representational geometry and bsMVPC accuracies. Quantification of these effects in

255   functional ROIs is illustrated in Fig S3. CHA significantly increased ISCs of

256   representational geometry in all ROIs (ROI mean ISCs = 0.308 and 0.210 after CHA

257   and anatomical alignment, respectively, difference = 0.097 [0.080, 0.110]). CHA also

258   dramatically increased bsMVPC accuracies in all ROIs (ROI mean bsMVPC accuracies =

259   10.37% and 1.04% after CHA and anatomical alignment, respectively, difference =

260   9.33% [7.71%, 10.54%]).

261

Fig 6. Effect of CHA on ISC or representational geometries and bsMVPC of movie data. (A) ISC

of representational geometry in each voxel mapped onto the cortical surface. (B) Accuracies for

bsMVPC of 15 s movie segments. Classification was performed within each movie half

separately, and the accuracies are then averaged across the two halves. Parameters for

hyperalignment are derived from the half that was not used for classification.

266   *Generalization to task maps from the HCP database*

267   We tested the generalization of the common model connectome derived from

268   resting state fMRI by applying connectivity hyperalignment parameters derived from

269   one session of resting state data to task maps provided by the HCP database

270   comprised of 32 task activation maps and 14 task contrast maps (Supplemental Table

271   S2). These task maps reflect simple operations and, thus, do not have the same

272   fine-grained structure that is associated with activation by dynamic, naturalistic stimuli

273   such as a movie. We calculated the ISC of these task maps between each subject and

274   the average of others before and after hyperalignment. Hyperalignment improved

275   correlations on average across all tasks and in all but two (Face-Shapes and

276   Body-Average, labeled ns) task contrast maps (Fig 7). The average correlation across

277   task maps increased from 0.58 to 0.65 (mean difference = 0.07 [0.06, 0.08]).

278   Figure 7.   ISCs of HCP task activation and contrast maps after CHA and surface alignment

279   (MSM-All).

280   *Comparison of CHA and Response Hyperalignment (RHA)*

281   Since CHA aligned fine-scale patterns of response tuning functions across

282   subjects better than anatomy-based alignment, we asked how well it compares to our

283   previously published response-based hyperalignment (RHA) [16]. Because RHA requires

284   responses that are synchronized across subjects in time, it cannot be applied to resting

285   state data. We compare CHA and RHA of movie viewing data on 1) ISC of connectivity

286   profiles, 2) ISC of representational geometry, and 3) bsMVPC of 15 s movie segments.

287   Results showed that both CHA and RHA increased ISCs and bsMVPC

288   classification accuracies significantly over anatomy-based alignment, but each

289   algorithm achieves better alignment for the information that it uses to derive a

290   common model, namely connectivity profiles and patterns of response, respectively.

291   ISCs of connectivity profiles are significantly higher in a common model based on CHA

292   than in a common model based on RHA (ROI mean ISCs = 0.67 and 0.575,

293   respectively; CHA-RHA difference = 0.095 [0.081, 0.112])(Supplemental Figure S2). By

294   contrast, RHA marginally but significantly outperforms CHA on some validations based

295   on response tuning functions, namely ISCs of representational geometry (ROI means =

296   0.322 and 0.308, respectively; RHA-CHA difference = 0.014 [0.007,

297   0.019])(Supplemental Figure S3), and bsMVPC of movie segments (ROI mean

298   accuracies = 13.65% and 10.37%, respectively; RHA-CHA difference = 3.28% [2.76%,

299   3.78%])(Supplemental Figure S4).

300   Discussion

301   These results show that fine-scale local variation in connectivity profile is a major

302   component of the human connectome that can be modeled with shared connectivity

303   basis functions. Each connectivity basis function has a connectivity profile that is

304   shared across subjects and a different local connectivity topography in each individual

305   brain. These basis functions are derived from multiple subject data in local cortical

306   fields. An individual's connectivity pattern in a cortical field is modeled as multiplexed

307   or overlaid connectivity topographic basis functions, and the connectivity profile of

308   each cortical node or voxel is modeled as a weighted mixture of local connectivity

309   profile basis functions. Thus, the connectivity profile for each voxel or node is modeled

310   as a high-dimensional vector of connectivity profile bases, capturing how it varies

311   locally from its neighbors, rather than modeling the connectivity of a brain area as a

312   single connectivity profile that is shared by all voxels or nodes. We show that these

313   shared basis functions can be discovered with connectivity hyperalignment of data

314   collected during viewing and listening to a rich naturalistic movie and during the

315   resting state. These basis functions constitute a common model connectome. Shared

316   fine-scale variation is a ubiquitous characteristic of all of human cortex and is a major

317   component of the human connectome that coexists with shared coarse-scale areal

318   variation.

319   We show that patterns of connectivity exhibit fine-scale variation that is captured

320   in the CHA-derived common model connectome. We define fine-scale structure as

321 voxel-by-voxel or node-by-node variation in response and connectivity profiles, as

322 compared to the coarse structure of parcels that consist of sets of voxels or surface

323 nodes and are treated as a functional unit with a homogeneous functional profile. In

324 Figure 8 we illustrate the fine scale structure that is captured in the common model

325 connectome for connectivity patterns in a left lateral-occipital/inferior-temporal cortex

326 cortical field. Quantitatively, we show that shared fine-scale structure is captured in the

327 common model connectome with a direct measure of the spatial granularity of local

328 variation in connectivity profiles — the intersubject point-spread function. The

329 intersubject spatial point-spread function for variation in connectivity profiles is

330 dramatically, six to eight-fold, steeper after data are transformed into the common

331 model connectome than for data that are anatomically aligned. Next we show that

332 capture of this fine-scale structure in functional connectivity generalizes to capture of

333 fine-scale structure in neural representation. Transformation of movie data into the

334 common model space, using matrices derived from functional connectivity in

335 independent movie data, afford bsMVPC of time segments that are tenfold higher than

336 for anatomically-aligned data. bsMVPC of movie time segments relies on fine-scale

337 structure that is not well-aligned based on anatomy, nor on functional alignment using

338 a "rubber-sheet" warping of cortical topographies, nor on hyperalignment based on

339 responses to a limited variety of still images of visual categories [13,16, 23-25]. ISCs of

340 local representational geometries also are dramatically higher after CHA than after

341 anatomical alignment. These local representational geometries reflect fine-scale

342 structure that reveals how information spaces in different cortical fields vary, offering a

343   window on how these spaces are transformed along processing pathways and

344   reshaped by task demands [26-28]. Finally, we also show that transformations derived

345   from rsfMRI improve alignment of topographies in task activation and task contrast

346   maps in the HCP database.

347

Figure 8. Mean group connectivity patterns in a left lateral-occipital/inferior temporal cortical field.

348   Connectivity patterns were measured from movie data for functional connectivity with connectivity

349   targets in mid lateral fusiform gyrus and mid superior temporal sulcus. Mean group connectivity

350   patterns are shown for data in the common model connectome, derived with CHA based on

351   responses to the other half of the movie, and for anatomically aligned data. Mean ISCs for patterns

352   after CHA are higher than after anatomical alignment for both the fusiform target (0.835 versus

353   0.175) and the STS target (0.826 versus 0.306). The occipitotemporal, mid fusiform, and mid STS

354   loci are taken from the face-responsive fields identified by Visconti di Oleggio Castello, Halchenko,

355   et al. [28]. The locations of the fusiform and STS targets are indicated with green and blue dots,

356   respectively. The inflated cortical surface is tipped to provide a clear view of the cortical field.

357   Connectivities are correlations of time-series responses to the movie.

358   The existence and importance of fine-scale connectivity is well-recognized

359   [29-31] but previously was not modeled in a common computational framework and,

360   consequently, was largely overlooked. Attempts to model within-area topographies of

361   connectivity either were limited mostly to within-subject analyses or coarser within-area

362   topographies that could be captured with anatomy-based alignment of group data

363   [31]. Consequently, when not simply overlooked, within-area variations in connectivity

364   profiles were usually analyzed as gradients that have a single cycle in a cortical area,

365   such as retinotopy or somatotopy [29-31].

366   Other models of shared structure in the human connectome have focused on

367   the identification of shared functional networks that can be identified with cluster

368   analysis (e.g. [5,32,33]) or independent components analysis (ICA; e.g. [19]). These

369   methods do not attempt to align the fine-scale structure within areas in these networks.

370   In some approaches, each voxel is assigned to one cluster or system and is, thereby,

371   associated with the time-series tuning function that characterizes that cluster

372   [5,8,32,33]. Approaches that use ICA, or related componential analyses such as PCA or

373   SVD, have the potential to capture node-by-node variation in connectivity profiles, but

374   implementations of these approaches have not adapted them to analyze this fine-scale

375   topographic structure. For example, dual regression could allow using group ICA as a

376   common space for modeling each voxel in an individual as a weighted sum of

377   independent components [34,35]. In practice, however, each voxel is characterized in

378   ICA analyses by the network to which it belongs, not as a mixture of multiplexed

379   functional topographies. Node-by-node local variation in connectivity topographies is

380   blurred in group analyses because individual variation on independent components is

381   projected into anatomically-aligned brains rather than into a single reference voxel

382   space to reveal shared fine-scale structure, as we do here. A novel approach by Langs

383   et al. [32,33] allows nodes to be assigned to different clusters in a common functional

384   connectivity embedding space independently of anatomical location. The

385   implementations of this method, however, do not attempt to discover shared fine-scale

386   structure, and the low dimensionality of the embedding space and small number of

387   clusters are probably insufficient to capture this level of detail.

388   Cortical functional architecture has multiplexed topographies at multiple spatial

389   scales. In primary visual cortex, retinotopy is multiplexed with ocular dominance

390   columns, edge orientation, spatial frequency, motion direction, and motion velocity,

391   among other low-level visual attributes [36,37]. Primary visual cortex sends coherent

392   projections to other visual areas where these topographies are recapitulated and

393   transformed, affording the emergence of more complex features, such as curvature,

394   texture, shape, color constancy, and biological motion; and, subsequently, even

395   higher-order attributes such as object categories, view-invariant face identity, and

396   species-invariant attributes of animals such as action categories and dangerousness

397   [12,15,26-28,38-40]. Similar transformations of multiplexed topographies characterize

398   other sensory modalities and, undoubtedly, supramodal cognitive operations.

399   Modeling inter-areal communication as a single value of connectivity strength sheds no

400   light on how information is transformed along cortical processing pathways to allow

401   high-order information to be disentangled from confounding attributes [41].

402   Multiplexed cortical topographies at multiple spatial scales can be modeled with

403   individual-specific topographic basis functions that have shared tuning profiles [13,16]

404   and shared connectivity profiles (as shown here). No previous model captured multiple

405   spatial scales of connectivity topographies with connectivity profiles that are shared

406   across brains. By capturing coarse- and fine-scale connectivity topographies with

407   shared basis functions, the common model connectome casts a bright light on the

408   dominant role of fine-scale connectivity patterns in the human connectome and opens

409   new territory for investigation of the network properties of cortical connectivity at finer

410 levels of detail. With this new perspective, inter-areal connectivity can be modeled as

411 more than a simple replication of global activity, as is the assumption underlying

412 existing approaches to modeling the connectome, but, instead, as information

413 processing operations in which functional topographies are transformed by projections

414 between areas.

415 ## Methods

416 ### Movie data: Raiders of the Lost Ark

417 We scanned 11 healthy young right-handed participants (4 females; Mean age:

418 24.6+/-3.7 years) during movie viewing. Participants had no history of neurological or

419 psychiatric illness. All had normal or corrected-to-normal vision. Informed consent was

420 collected in accordance with the procedures set by the local Committee for the

421 Protection of Human Subjects. Participants were paid for their participation. These

422 data also were used in a prior publication on whole cortex RHA [16].

423 *Stimuli and design.* Stimuli consisted of the full-length feature movie — "Raiders of the

424 Lost Ark" — divided into eight parts of approximately 14 to 15 min duration. Video was

425 projected onto a rear projection screen with an LCD projector which the subject viewed

426 through a mirror on the head coil. The video image subtended a visual angle of

427 approximately 22.7° horizontally and 17° vertically. Audio was presented through MR

428 Confon's MRI-compatible headphones. Participants were instructed to pay attention to

429 the movie and enjoy. See [16] for details.

430 *fMRI protocol.* Participants were scanned in a Philips Intera Achieva 3T scanner with an

431 8 channel head coil at the Dartmouth Brain Imaging Center. T1-weighted anatomical

432　scans were acquired at the end of each session (MPRAGE, TR=9.85 s, TE=4.53 s, flip

433　angle=8°, 256 × 256 matrix, FOV=240 mm, 160 1 mm thick sagittal slices). The voxel

434　resolution was 0.9375 mm × 0.9375 mm × 1.0 mm. Functional scans of the whole brain

435　were acquired with an echo planar imaging sequence (TR=2.5 s, TE=35 ms, flip

436　angle=90°, 80 × 80 matrix, FOV=240 mm × 240 mm) every 2.5 s with whole brain

437　coverage (41 3 mm thick interleaved axial slices, giving isotropic 3 mm × 3 mm × 3 mm

438　voxels). We acquired a total of 2718 functional scans with 1350 TRs in four runs during

439　the first session and 1368 TRs in four runs during the second session.

440　*fMRI data preprocessing.* fMRI movie data were preprocessed using AFNI software

441　[42](http://afni.nimh.nih.gov). Functional data were first corrected for the order of slice

442　acquisition and head motion by aligning to the last volume of the last functional run.

443　Any spikes in the data were removed using 3dDespike in AFNI. Data were then filtered

444　using 3dBandpass in AFNI to remove any temporal signal variation slower than 0.00667

445　Hz, faster than 0.1 Hz or that correlated with the whole brain average signal or the

446　head movement parameters. Each subject's anatomical volume was first aligned to the

447　motion corrected average EPI volume and then to the MNI 152 brain template in AFNI.

448　Functional EPI BOLD data were then aligned to the MNI 152 brain template using

449　nearest neighbor resampling by applying the transformation derived from the

450　alignment of the anatomical volume to the template. Data acquired during the

451　overlapping movie segments were discarded resulting in a total of 2662 TRs with 1326

452　TRs in the first session and 1336 TRs in the second session.

453　*Definition of masks and searchlights for movie data.* We derived a gray matter mask by

454   segmenting the MNI_avg152T1 brain provided in AFNI and removing any voxel that

455   was outside the cortical surface by more than twice the thickness of the gray matter at

456   each surface node. It included 54,034 3 mm isotropic voxels across both hemispheres.

457   We used this mask for all subsequent analyses of all subjects.

458   Hyperalignment of movie data started with hyperalignment of data in 20,484

459   overlapping searchlights of 20 mm radius centered on cortical nodes with 2.9 mm

460   average spacing between the nodes. Cortical nodes were defined in a standard

461   cortical surface from FreeSurfer (fsaverage)(https://surfer.nmr.mgh.harvard.edu) and

462   resampled into a regular grid using AFNI's MapIcosahedron [42,43] with 10,242 nodes

463   in each hemisphere. We defined the surface searchlights [44] in PyMVPA

464   [45](http://www.pymvpa.org) as cortical disks. The thickness of disks was extended

465   beyond the gray matter, as defined in FreeSurfer, 1.5 times inside the white-matter

466   gray-matter boundary and 1.0 times outside the gray-matter pial surface boundary to

467   accommodate any misalignment of gray matter as computed from the anatomical scan

468   and the gray matter voxels in the EPI scan. To reduce the contribution from noisy or

469   non-gray matter voxels that were included due to this dilation, we used a

470   between-subject correlation measure on training data [13] to select 70% of the voxels

471   in each searchlight [16]. The mean number of selected voxels in movie data

472   searchlights was 235.

473   Searchlights for defining connectivity targets were defined using a coarse

474   surface grid corresponding to the ico8 surface in SUMA [43] with 1284 nodes (10.7 mm

475   spacing between nodes). We used surface disk searchlights [44] centered on these

476   nodes as the movie data connectivity target searchlights. These searchlights had a

477   radius of 13 mm, as did those used for the HCP data, producing complete coverage of

478   the cortex with overlapping searchlights. Cortical disks centered on these voxels were

479   dilated using the same procedure as for hyperalignment of cortical surface searchlights.

480   Movie connectivity target searchlights had a mean of 99 voxels.

481

Resting state data: Human Connectome Project

482   In the HCP database [20], we found unrelated subjects of age <= 35 with at least

483   four resting state scans, yielding a list of 64 subjects. We chose the first 20 of these

484   subjects in the sorted order of subject IDs for our analysis.

485   For each subject, we used their cortical surfaces and fMRI data aligned to the

486   group using MSM-All [22] with 32K nodes in each hemisphere as provided by the HCP.

487   We used data from one resting state session [19]("rfMRI_REST1_LR") to derive CHA

488   parameters and validated it on a different resting state session ("rfMRI_REST2_LR"),

489   and task fMRI sessions [18](EMOTION, GAMBLING, LANGUAGE, MOTOR,

490   RELATIONAL, SOCIAL, and WM). Resting state data were acquired for 1200 TRs with a

491   TR of 0.720s in each session (total time=14 min 33 s). The data used to derive the CHA

492   parameters and common model and the resting state data used for validation tests

493   used the same phase-encoding direction (LR). We used a single session of rsfMRI for

494   alignment to mimic a typical resting state data acquisition which usually varies from

495   10-20 mins of scanning. See [19] for more details about the acquisition and

496   preprocessing pipelines.

497   *Definition of masks and searchlights for HCP data.* We masked the data to include only

498   the left and right cortices (Cortex_Left and Cortex_Right), removing all the non-zero

499   nodes that correspond to the medial subcortical regions, resulting in 59,412 nodes

500   across both hemispheres. These nodes also defined the centers of 59,412 surface

501   searchlights [44] with 20 mm radii that were used for hyperalignment. All nodes in

502   these searchlights were included. The mean number of surface nodes in the HCP

503   searchlights was 337.

504   We defined connectivity target searchlights using a coarser surface grid

505   corresponding to the ico8 surface in SUMA [43] with 1284 nodes (10.7 mm spacing

506   between nodes). We found the closest matching nodes on the 32K surface to the

507   nodes on the ico8 surface, and used those as centers for connectivity target

508   searchlights. These searchlights had a radius of 13 mm, producing complete coverage

509   of the cortex with overlapping searchlights. HCP connectivity target searchlights had a

510   mean of 142 loci. See further details below for how time-series were extracted from

511   these searchlights.

512   For validation of task fMRI, we used all of the maps provided by the HCP after

513   removing redundancies (such as FACE-AVG and AVG-FACE), which resulted in 46 maps

514   (Supplemental Table S2).

515

Connectivity Hyperalignment

516   We use CHA to derive a common model of the human connectome and the

517   transformation matrices that project individual brains' connectomes into the common

518   model connectome space. The common model connectome is a high-dimensional

519   information space. In the current implementation, the model space based on movie

520   fMRI data has 54,034 dimensions, corresponding to the number of voxels in the gray

521   matter mask, and the model space based on HCP resting state fMRI data has 59,412

522   dimensions, corresponding to the number of cortical nodes in those data. The

523   derivation of this space starts with hyperalignment in local cortical fields, searchlights,

524   which yields orthogonal transformation matrices for each subject in each field. These

525   searchlights are aligned across subjects based on anatomy (movie data) or MSM-All

526   (HCP resting state data); consequently, each locus within a searchlight is similarly

527   aligned across subjects before CHA. Local transformation matrices for each searchlight

528   map anatomically or MSM-All aligned cortical loci in a cortical field to CHA-aligned

529   dimensions in the common model connectome. These local transformation matrices

530   are then aggregated into a whole brain transformation matrix, which is not globally

531   orthogonal. The whole brain transformation matrices are derived based on local

532   hyperalignment in searchlights to constrain resampling of information to cortical

533   neighborhoods defined by those searchlights.

534

The basic equation for hyperalignment (both CHA and RHA). B_{ij} are the original

535   matrices of data for cortical fields, j, in individual brains, i, which have m_{ij} columns of

536   cortical loci and n rows of data vectors. Hyperalignment derives a transformation

537   matrix for each cortical field in each individual, R_{ij}, and a matrix for each cortical field,

538   M_j, that is the mean of transformed individual brain matrices, $B_{ij}R_{ij}$, minimizing the

539   Frobenius norm of differences between transformed individual brain matrices and the

540   model space matrix. For each cortical field j:

541

equation 1. $\qquad M_j = (1/N) \sum_{i=1}^{N} (B_{ij} R_{ij})$ where $\quad R_{ij} = argmin_R \sum_{i=1}^{N} \|B_{ij} R - M_j\|_F$

542   For whole cortex hyperalignment we define the cortical fields, j, as searchlights.

543   Thus, we estimate a transformation matrix, R_{ij}, for each of N_{sl} searchlights in each

544   subject i. We then aggregate these searchlight transformation matrices into a whole

545   cortex transformation matrix, R_{iA} (details below):

546   equation 2. $\qquad R_{iA} = f(R_{ij})$

547   The whole cortex common model data matrix, M, is created by transforming

548   individual whole cortex data matrices, B_{iA}, into common model space coordinates and

549   calculating the mean:

550

equation 3. $\qquad M = (1/N) \sum_{i=1}^{N} (B_{iA} R_{iA})$

551   Conversely, other subjects' data in the common model space can be mapped

552   into any subject's individual anatomical space using the transpose of that subject's

553

whole cortex transformation matrix, R_{iA}^T, producing a data matrix, M_i, in which the

554   columns are that subject's cortical loci, making it possible to analyze and visualize

555   transformed group data in any subject's anatomical space:

556

equation 4. $M_i = M R_{iA}^T$

557   In our implementations of hyperalignment, we have used a variant of

558   Generalized Procrustes Analysis [46,47](described in detail below) to derive orthogonal

559   transformation matrices for the improper rotations of a brain data matrix from a cortical

560   field (region of interest or searchlight) to the mean of others' matrices for the same

561   region to minimize interindividual differences between the transformed individual and

562   mean data matrices. Aggregation of searchlight transformation matrices, R_{ij}, produces

563   a whole cortex transformation matrix, R_{iA}. Because R_{iA} is derived from searchlight

564   transformation matrices, R_{ij}, it imposes a locality constraint that limits remapping of

565   brain data to nearby cortical loci (see details below), making the whole cortex

566   transformation matrix nonorthogonal by design. We also have tested other

567   hyperalignment algorithms that use alternatives for calculating the transformation

568   matrices, such as regularized canonical correlation and probabilistic estimation [48,49].

569   These alternatives are effective but have not yet been extended to aggregate local

570   transformation matrices for cortical fields into a whole cortex transformation matrix.

571   The dimensionality of the brain and model data matrices is $n \times m$, in which m

572   equals the number of cortical nodes or dimensions in brain and model data matrices —

573   B_{ij}, B_{iA}, M_j, and M — and n equals the number of data vectors across these

574   dimensions. The number of data vectors, n, is set and determined by the number of

575   connectivity targets for defining connectivity pattern vectors (see details below). For

576   RHA, n is set by the number of response pattern vectors in an experimental dataset.

577   The number of cortical loci in a cortical field or searchlight, m_{ij}, can vary across

578   subjects. If the number of cortical loci or dimensions differs between subjects or

579   between an individual subject and the model space, the new subject's data are

580   transformed into a space with the same dimensionality as the first subject's or the

581   model's space. The number of cortical loci in the whole cortex model is set at $m = $

582   59,412 for HCP data and $m = 54,034$ for movie data. We also have shown that the

583   dimensionality of a model for region of interest or searchlight (m_j) can be reduced

584   substantially relative to the dimensionality of individual brain spaces in imaging

585   datasets (m_{ij}), $m_{Mj} << m_{ij}$ [13,16,48]. In the current version of CHA, as in whole cortex

586   RHA, however, we do not reduce the dimensionality of the model space because these

587   reduced dimensionality local models are difficult to aggregate into a whole cortex

588   model.

589   Note that the common model data matrix has two distinct components. The

590   columns define a common model space, whereas the rows are defined by the

591   experimental data — either patterns of connectivity to targets elsewhere in the brain

592   for CHA, or patterns of response for RHA. The space can be illustrated as an

593   anatomical space insofar as it can be rotated into any individual's cortical loci (equation

594   4), but there is no "canonical" anatomical space, rather the individuality of each

595   individual brain is preserved. We illustrate results in the anatomical space of one

596   subject, the "reference subject", but we also could illustrate the results in other

597   subjects' anatomical spaces. The special nature of the common space derives from the

598   alignment of functional indices — connectivities and responses — to minimize

599   interindividual differences and, thereby, discover shared basis functions for the

600   individually variable functional architecture. These basis functions are the response and

601   connectivity profiles for model dimensions that model the response and connectivity

602   profiles of cortical loci in individual brains as linear weighted sums. In other words,

603   equation 4 models single columns in B_i as weighted sums of columns in M_i.

604   Transformation matrices consist only of weights for the projection of individual

605   brain spaces for cortical fields, B_{ij}, or the whole cortex, B_{iA}, into model spaces (M_j, M)

606   and contain no connectivity or response data. Thus, a transformation matrix can be

607   applied to any matrix of data vectors in an individual brain space. Similarly, the

608

       transposes of transformation matrices, R_{iA}^T , can be applied to any data vector in the

609   model space to project that vector into the cortical topographies of individual brains.

610   For all applications of the common model, including the validation tests presented

611   here, the transformation matrices are applied to independent data that played no role

612   in derivation of the model space and the individual transformation matrix parameters.

613   This is necessary to avoid overfitting [50]. Transformation matrices derived from

614   connectivity data also can be applied to response data and vice versa. In other words,

615   RHA and CHA are complementary methods for deriving a common model of

616   information spaces in cortex, and RHA-derived and CHA-derived transformation

617   matrices are alternative projections for mapping individual brain data into the same

618   common model space. Note that each column of the transformation matrix R_{iA}

619   contains weights for cortical loci in subject i's brain. These columns of weights are

620   basis functions for modeling functional topographies in individual brains as linear

621   weighted sums of topographies associated with model dimension functional profiles.

622

Derivation of transformation matrices for regions of interest and searchlights. The

623   derivation of individual transformation matrices that map individual brain spaces into

624   the common model space is a three-level iterative process.   We present the iterative

625   algorithm for deriving transformation matrices and the common model space in greater

626   detail here to help readers understand better its structure.

627   In the first step of the first level, the data matrix for a cortical field in one subject,

628   B_{2j}, is transformed to be in optimal alignment with the same cortical field in another

629   subject's brain, B_{1j}, referred to here as the reference subject:

630

equation 5. $argmin \lVert B_{2j} R_{2j(level1)} - B_{1j} \rVert_F$

631   We use the Procrustes transformation to find the orthogonal matrix that affords

632   the optimal improper rotation to achieve this minimization [46]. Note that this

633   "rotation" is a rotation of data in the high-dimensional feature space, not a rotation in a

634   two or three dimensional anatomical space. Elsewhere we have shown that other

635   algorithms can be used to achieve this minimization [48,49].

636   In the following steps of the first level, the brain data matrices for the third and

637   subsequent subjects are transformed to be in optimal alignment with the matrix

638   defined by the mean of the previous subject's matrix and the previous mean:

639

equation 6. $\qquad argmin \, \|B_{ij}R_{ij(level1)} - M_{i-1j(level1)}\|_F$

640   where

641

equation 7. $\qquad M_{i-1,j(level1)} = (B_{i-1,j}R_{i-1,j(level1)} + M_{i-2,j(level1)})/2$

642    $M_{i-1,j(level1)}$ is the target data used to hyperalign the current subject's data, B_{ij},

643   and $M_{i-2,j(level1)}$ is the target data used to hyperalign the previous subject's data, $B_{i-1,j}$.

644   Target data is updated with previous subjects' aligned data in this first level. In the

645   subsequent two levels each subject's data matrix is hyperaligned to the simple,

646   unweighted mean of all other subjects' matrices.

647   At the end of the first level, level one transformation matrices have been derived

648   for all cortical fields in all subjects, $R_{i,j(level1)}$, which are used to project each subjects'

649   brain data into the provisional common spaces that evolved over level one iterations

650    $M_{i,j(level1)}$. Each subject is then re-hyperaligned to the mean data matrix for all other

651   subjects' transformed data from level one to derive new individual transformation

652   matrices, $R_{ij(level2)}$. Note that the new transformation matrices are derived using each

653   subject's original brain data, B_{ij}. Note also that the mean matrices in provisional

654

common spaces, $M_{\neg i,j(level1)}$, exclude data from the subject being hyperaligned:

655

equation 8.
$$argmin \sum_{i=1}^{N} \left\| B_{ij} R_{ij(level2)} - M_{\neg i,j(level1)} \right\|_{F}$$

656

where $M_{\neg i,j(level1)}$ is the equally-weighted mean of level one transformed data for all

657   subjects but subject i:

658

equation 9.
$$M_{\neg i,j(level1)} = (1/(N-1)) \sum_{k=1(\neg i)}^{N} (B_{kj} R_{kj(level1)})$$

659   After the level two transformation matrices, $R_{ij(level2)}$, are calculated for each

660   subject, the level one transformation matrices are discarded, and the group mean of

661   transformed individual brain data matrices is recalculated, using these new

662   transformation matrices, producing the model matrix, M:

663

equation 10.
$$M_j = (1/N) \sum_{i=1}^{N} B_{ij} R_{ij(level2)}$$

664   In level 3, the last level, the final searchlight transformation matrices, R_{ij}, are

665   recalculated for each subject (see equation 1 above).

666

Derivation of whole cortex transformation matrices. Orthogonal transformation

667   matrices for hyperaligning a cortical field can map information from a cortical locus into

668   model dimensions anywhere else in that cortical field. To constrain the remapping of

669   information to nearby locations in the reference subject's cortical anatomy, we

670   developed a searchlight-based approach [16]. We hyperalign the data in N_{sl}

671   overlapping searchlights, where N_{sl} is the number of searchlights (59,412 for HCP data,

672   20,484 for movie data). The number of model dimensions in each searchlight

673   transformation matrix is determined in the movie data by cortical location and the

674   number of selected features in the reference subject (mean = 235) and in HCP data by

675   the cortical location of the searchlight (mean = 337). The transformation for each

676   searchlight, R_{ij}, has dimensionality that corresponds to the number of nodes in an

677   individual's searchlight (m_{ij} rows) and the number model dimensions in that searchlight,

678   derived from the reference subject's anatomy (m_{1j} rows). Thus, each transformation

679   matrix has on the order of 28K and 57K free parameters for movie data and HCP data,

680   respectively. Because the searchlights are overlapping, there are multiple estimates of

681   weights for mapping each cortical locus to each model dimension. As described in

682   Guntupalli et al. [16] these weights are aggregated across searchlights by adding all

683   weights for each cortical-locus-to-model-dimension mapping. In essence, this is

684   equivalent to creating a whole cortex transformation matrix, R_{iA}, of dimensionality $m \times$

685   m, by padding each searchlight transformation matrix, R_{ij}, with zeroes in all rows and

686   columns for cortical loci and model dimensions that are not in the individual or model

687   searchlight cortical field to give them the same dimensionality to produce $R_{ij(padded)}$,

688   and then summing these padded transformation matrices. Thus, for each subject, i:

689

equation 11. $$R_{iA} = \sum_{j=1}^{N_{sl}} R_{ij(padded)}$$

690   where N_{sl} is the number of searchlights and $R_{ij(padded)}$ is the padded transformation

691   matrix for subject i in searchlight j with dimensionality $m \times m$. As noted above, m is

692   the number of cortical loci — 59,412 surface nodes for HCP data and 54,034 voxels in

693   the gray matter mask for movie data — and the number of whole cortex model

694   dimensions. Because the searchlight approach constrains

695   cortical-locus-to-model-dimension mapping to nearby cortical locations, the whole

696   cortex transformation matrix, R_{iA}, is sparse with zero weights for all mappings of

697   cortical loci to model dimensions that are separated by more than 2x the searchlight

698   diameter (~4 cm in this implementation). The whole cortex transformation matrices,

699   R_{iA}, are large ($m \times m$) but sparse. 98.7% of the entries are zeros, and roughly 20 million

700   entries have nonzero values in each of these matrices. The additive aggregation of

701   mapping parameters weights nearby cortical location pairs, which co-occur in more

702   searchlights than distant pairs, more strongly than distant pairs, adding a further locality

703   constraint. Note that the searchlight transformation matrices, R_{ij}, are orthogonal but

704   the whole cortex transformation matrices, R_{iA}, are not by design, to introduce the

705   locality constraint. The whole cortex transformation matrices, R_{iA}, are used in all

706   validation tests to hyperalign independent new data matrices after normalizing the

707   data in each cortical node or voxel. In other words, all validation tests are performed

708   on independent data that played no role in deriving the transformation matrix

709   parameters or the common model connectome, providing cross-validated

710   generalization testing. CHA of movie data was based on one half of the movie data

711   (~55 min, ~1300 TRs) and the other, independent half of the movie data was used for

712   validation tests with two-fold cross-validation. CHA of HCP data was based on one

713   session of resting state data (~15 min, 1200 TRs) and a second session of independent

714   resting state data was used for validation tests, as well as independent data from task

715   fMRI [18].

716   Note that transformations map the cortical loci of a subject's data matrices

717   (columns) into the reference subject's cortical loci. Thus, we use the reference subject's

718   cortex for illustration, but note that the anatomical coordinates for model dimensions

719   are an abstraction, as even the reference subject's data are mapped into model space

720   coordinates with a transformation matrix that is not the identity matrix.   Data matrices

721   in the model space also can be mapped into any subject's cortical anatomy by using

722   the transpose of that subject's transformation matrix (equation 4). Thus, the

723   hyperaligned data in the common model space can be illustrated in any subject's

724   anatomical space. The anatomical space that we use for illustration, that of the

725   reference subject, should not be considered a canonical space but, rather, simply as

726   one of many possible physical instantiations.

727

      Connectivity targets.   We define functional connectivities as the correlations of the

728   response profiles — series of responses across time — of cortical loci or dimensions

729   with the response profiles of targets (t_j) distributed across the cortex. We use two sets

730   of connectivity targets, one reduced set to derive the transformation matrices and

731   common model connectivity data matrix, and a more complete set to test the validity

732   of the model. We define a reduced set of connectivity targets using surface-searchlight

733   target ROIs to make derivation of the model more computationally tractable, as

734   compared to using all cortical loci as individual connectivity targets. For the reduced

735   set, we use 3852 targets (top 3 components for 1284 searchlights; note that the

736   searchlights for connectivity targets are different from the searchlights that are

737   hyperaligned as described above in the Resting State Data and Movie Data sections;

738   see details for defining searchlight PC connectivity targets in the next section). For

739   validation testing we analyze the full connectome, defining connectivity targets as all

740   cortical loci in the brain (N_{cl} = 54,034 gray matter voxels in the movie data and 59,412

741   cortical nodes in the HCP resting state data).

742

Searchlight ROI connectivity targets. Each surface-searchlight connectivity target has a

743   radius of 13 mm and is centered on a node of a coarse surface with a total of 1284

744   nodes covering both hemispheres. Thus, neighboring connectivity targets searchlights

745   are overlapping. Unlike others (e.g., [5]) we do not assume that a searchlight

746   connectivity target has a single response profile. We find, rather, a variety of response

747   profiles for individual cortical loci in a target searchlight that can be captured as

748   principal components.   We used the top three principal components to represent the

749   response profiles in a target searchlight.

750   To insure that the top components in target searchlights capture the same

751   connectivity patterns across subjects, we performed a singular value decomposition

752   (SVD) on the group mean connectivity matrix for each target searchlight after a

753   simplified hyperalignment of individual matrices. Note that using a naive PCA/SVD to

754   derive top components in each subject's searchlight independently will not guarantee

755   their functional similarity. Target searchlights had a mean of 142 loci (HCP data) or 99

756   voxels (movie data). At this stage it was not yet possible to break the response profiles

757   for searchlight targets into multiple components with shared connectivity profiles.

758   Consequently, connectivity targets for the procedure to derive these components were

759   simply the mean time-series responses for target searchlights. For each target

760   searchlight with N_s features (surface nodes or voxels), we computed a 1284 × N_s

761   correlation matrix (the correlations between each cortical locus in the target searchlight

762   and the mean time series for all target searchlights) for each subject. We hyperaligned

763   the features (cortical loci) in each target searchlight across subjects based on these

764   matrices and calculated the mean correlation matrix after hyperalignment in each

765   target searchlight. We then performed a singular value decomposition (SVD) of each

766   searchlight's group mean matrix to obtain the top three components that explained the

767   most shared variance. Each of these components is a weighted sum of cortical loci in a

768   target searchlight for each subject, and these weights afford calculation of a time-series

769   response whose connectivity profile with other targets is shared across subjects. Each

770   individual subject's time-series responses for the top three components were then used

771   as target response profiles for CHA. This step gave us 1284 × 3 = 3852 target response

772   profiles in each subject's cortex.

773

Validation tests and statistical analyses

774   *Functional ROIs.* In addition to analyzing the results of validation tests in each feature

775   or searchlight across the whole cortex, we also examined the results of validation tests

776   in functional ROIs associated with different sensory, perceptual, and cognitive functions

777   to assess the general validity of the common model [16]. We searched for terms and

778   cortical areas implicated in visual, auditory, cognitive, and social functions in

779   NeuroSynth [22] and took the coordinates for the peak location associated with each of

780   24 terms (Supplementary Table 1). For validation testing using the movie dataset, we

781   used volume searchlights centered around those peak loci with a radius of 3 voxels as

782   our functional ROIs. For validation testing using the HCP dataset, we found the closest

783   surface node corresponding to each peak locus and used a surface searchlight with a

784   10 mm radius around that surface node as the functional ROI. Functional ROIs that

785   were medial and encompassing both hemispheres in the volume space were split into

786   left and right ROIs in the surface space resulting in 26 ROIs for tests on the HCP data.

787   For analyses of ISCs and PSFs of connectivity profiles in functional ROIs, we calculated

788   the mean ISC or PSF across all cortical loci within the ROI searchlights (Figs. 3C, 4D,

789   5A, and 5C).

790
       Statistics. We used bootstrapping to test for significance of the contrasts between

791   alignment methods by sampling subjects 10,000 times to compute 95% CIs using

792   BootES [51]. We did this for each ROI and for the mean of all ROIs separately. We used

793   the same bootstrapping procedure for all validation tests unless specified otherwise.

794
       Control for effect of filtering. In addition to the anatomically-aligned movie data and

795   MSM-All aligned HCP resting state fMRI data, we calculated a third dataset that

796   controls for the effect of filtering the data through CHA transformations but aligns

797   those filtered data across subjects based on anatomical or MSM-All alignment. To

798   produce the filter control data, we created multiple common model connectomes

799   using each subject as the reference. Each subject's connectome was transformed into

800   the common connectome whose reference subject was the next subject in our order of

801   subjects. The last subject's connectome was transformed into the common model

802   connectome whose reference brain was that of the first subject. Thus, each subject's

803   connectome is filtered by hyperalignment, but since the common model connectome

804   for each subject has a different reference, the correspondence across filtered

805   connectomes is based only on anatomical alignment and preserves the anatomical

806   variability in the movie data and HCP datasets.

807

Intersubject correlation (ISC) of connectivity profile vectors. For validity testing we

808   applied a more detailed definition of the connectome to measure fine-grained

809   structure. The connectivity profile vector for a feature (or a cortical node or voxel) was

810   defined as the correlation of its time-series with of all other cortical nodes or voxels.

811   ISCs of connectivity profiles were computed between each subject's connectivity

812   profiles and the average connectivity profiles of all other subjects in each cortical locus.

813   For the movie data ISCs of connectivity profiles were computed within each

814   movie half separately and before and after CHA based on the other half of the movie.

815   Correlation values were Fisher transformed before averaging across both halves of the

816   movie in each voxel. These were then averaged across all subjects and inverse Fisher

817   transformed before mapping onto the cortical surface for visualization. ISCs of resting

818   state connectivity profiles were computed for session REST2. Session REST1 was used

819   for deriving the common model connectome and transformation matrices. ISCs were

820   calculated for data mapped into the common model connectome, for movie data

821   aligned anatomically, for HCP resting state data aligned with MSM-All, and for filter

822   control movie and HCP data.

823   We also computed within-subject between-session (REST1 and REST2)

824   correlation of resting state connectivity profiles. Within-subject between-sessions

825   correlations were calculated on data that are transformed by CHA as used for our main

826   analyses.

827

       Spatial point spread function. To investigate the spatial granularity of representation,

828   we computed a spatial point spread function (PSF) of ISCs or WSCs of connectivity

829   profiles. We computed the correlation of connectivity profiles in each cortical locus

830   (surface node or voxel) with the average connectivity profiles of cortical loci at varying

831   cortical distances in other subjects' data. To account for the effect of filtering, we did

832   this analyses with filter control data that were filtered with CHA but aligned based on

833   anatomy and MSM-All and after CHA with each subject aligned to the same reference

834   subject [16]. We computed similar PSFs for connectivity profiles within-subject

835   between-sessions (REST1 and REST2). This was also performed after CHA to account

836   for any filtering effects but to a single common space as used for our main analyses.

837

       ISC of representational geometry. ISCs of similarity structures were computed within

838   each movie half separately using a searchlight of 3 voxel radius. The mean number of

839   voxels in these searchlights was 102. In each searchlight, similarity structure was

840   computed as a matrix of correlation coefficients between patterns of response for every

841   pair of time-points from that movie half for each subject. The flattened upper triangle

842   of this matrix excluding the diagonal was extracted as the profile of representational

843   geometry at each searchlight for each subject. ISC of representational geometry in

844   each searchlight was computed as the correlation between each subject's

845   representational geometry and the average of all other subjects' representational

846   geometries for that searchlight. Correlation values were Fisher transformed before

847   averaging across both movie halves in each voxel. These were then averaged across all

848   subject-average pairs and inverse Fisher transformed before mapping onto the cortical

849   surface for visualization. The same steps were performed to compute inter-subject

850   correlation of representational similarity before and after hyperalignment.

851

       Between-subject multivariate pattern classification (bsMVPC). bsMVPC of 15 s movie

852   time segments (6 TRs) was computed within each movie half separately using

853   searchlights of 3 voxel radius, as in the analysis of representational geometry. bsMVPC

854   was performed using a one-nearest neighbor classifier based on correlation distance

855   [12,16]. Each 15 s (6TR) sequence of brain data for an individual was compared to other

856   subjects' mean responses to that sequence and all other 15 s sequences in the same

857   movie half using a sliding time window, resulting in over 1300 alternative time

858   segments (chance classification accuracy < 0.1%). Classification accuracies in each

859   searchlight were averaged across both halves in each subject before mapping the

860   subject means onto searchlight center voxels on the cortical surface for visualization.

861   We implemented our methods and ran our analyses in PyMVPA

862   [45](http://www.pymvpa.org) unless otherwise specified. All preprocessing and analyses

863   were carried out on a 64-bit Debian 7.0 (wheezy) system with additional software from

864   NeuroDebian [52](http://neuro.debian.net).

865

Acknowledgements

875   References

876   1. Biswal B, Yetkin FZ, Haughton VM, Hyde JS. Functional connectivity in the motor

877   cortex of resting human brain using echo-planar MRI. Magn Reson Med. 1995;34:

878   537–541.

879   2. Smith SM, Vidaurre D, Beckmann CF, Glasser MF, Jenkinson M, Miller KL, et al.

880   Functional connectomics from resting-state fMRI. Trends in Cognitive Sciences.

881   2013;17: 666–682.

882   3. Hutchison RM, Womelsdorf T, Allen EA, Bandettini PA, Calhoun VD, Corbetta M, et

883   al. Dynamic functional connectivity: Promise, issues, and interpretations.

884   NeuroImage. 2013;80: 360–378.

885   4. Sporns O, Chialvo DR, Kaiser M, Hilgetag CC. Organization, development and

886   function of complex brain networks. Trends in Cognitive Sciences. 2004;8: 418–425.

887   5. Thomas Yeo BT, Krienen FM, Sepulcre J, Sabuncu MR, Lashkari D, Hollinshead M, et

888   al. The organization of the human cerebral cortex estimated by intrinsic functional

889   connectivity. Journal of Neurophysiology. 2011;106: 1125–1165.

890   6. Wig GS, Laumann TO, Cohen AL, Power JD, Nelson SM, Glasser MF, et al.

891   Parcellating an Individual Subject's Cortical and Subcortical Brain Structures Using

892   Snowball Sampling of Resting-State Correlations. Cereb Cortex. 2014;24:

893   2036–2054.

894   7. Laumann TO, Gordon EM, Adeyemo B, Snyder AZ, Joo SJ, Chen M-Y, et al.

895   Functional System and Areal Organization of a Highly Sampled Individual Human

896   Brain. Neuron. 2015;87: 657–670.

897   8. Gordon EM, Laumann TO, Adeyemo B, Petersen SE. Individual Variability of the

898   System-Level Organization of the Human Brain. Cereb Cortex. 2017;27: 386–399.

899   9. Glasser MF, Coalson TS, Robinson EC, Hacker CD, Harwell J, Yacoub E, et al. A

900   multi-modal parcellation of human cerebral cortex. Nature. 2016;536: 171–178.

901   10. Gordon EM, Laumann TO, Adeyemo B, Huckins JF, Kelley WM, Petersen SE.

902   Generation and Evaluation of a Cortical Area Parcellation from Resting-State

903   Correlations. Cereb Cortex. 2016;26: 288–303.

904   11. Cohen AL, Fair DA, Dosenbach NUF, Miezin FM, Dierker D, Van Essen DC, et al.

905   Defining functional areas in individual human brains using resting functional

906   connectivity MRI. NeuroImage. 2008;41: 45–57.

907   12. Haxby JV, Gobbini MI, Furey ML, Ishai A, Schouten JL, Pietrini P. Distributed and

908   Overlapping Representations of Faces and Objects in Ventral Temporal Cortex.

909   Science. 2001;293: 2425–2430.

910   13. Haxby JV, Guntupalli JS, Connolly AC, Halchenko YO, Conroy BR, Gobbini MI, et

911   al. A Common, High-Dimensional Model of the Representational Space in Human

912   Ventral Temporal Cortex. Neuron. 2011;72: 404–416.

913   14. Haxby JV, Connolly AC, Guntupalli JS. Decoding Neural Representational Spaces

914   Using Multivariate Pattern Analysis. Annual Review of Neuroscience. 2014;37:

915   435–456.

916   15. Grill-Spector K, Weiner KS. The functional architecture of the ventral temporal

917   cortex and its role in categorization. Nat Rev Neurosci. 2014;15: 536–548.

918   16. Guntupalli JS, Hanke M, Halchenko YO, Connolly AC, Ramadge PJ, Haxby JV. A

919   Model of Representational Spaces in Human Cortex. Cereb Cortex. 2016;26:

920   2919–2934.

921   17. Norman KA, Polyn SM, Detre GJ, Haxby JV. Beyond mind-reading: multi-voxel

922   pattern analysis of fMRI data. Trends in Cognitive Sciences. 2006;10: 424–430.

923   18. Barch DM, Burgess GC, Harms MP, Petersen SE, Schlaggar BL, Corbetta M, et al.

924   Function in the human connectome: Task-fMRI and individual differences in

925   behavior. NeuroImage. 2013;80: 169–189.

926   19. Smith SM, Beckmann CF, Andersson J, Auerbach EJ, Bijsterbosch J, Douaud G, et

927   al. Resting-state fMRI in the Human Connectome Project. NeuroImage. 2013;80:

928   144–168.

929   20. Van Essen DC, Smith SM, Barch DM, Behrens TEJ, Yacoub E, Ugurbil K. The

930   WU-Minn Human Connectome Project: An overview. NeuroImage. 2013;80: 62–79.

931   21. Yarkoni T, Poldrack RA, Nichols TE, Essen DCV, Wager TD. Large-scale automated

932   synthesis of human functional neuroimaging data. Nature Methods. 2011;8:

933   665–670.

934   22. Robinson EC, Jbabdi S, Glasser MF, Andersson J, Burgess GC, Harms MP, et al.

935   MSM: A new flexible framework for Multimodal Surface Matching. NeuroImage.

936   2014;100: 414–426.

937   23. Sabuncu M, Singer BD, Conroy B, Bryan RE, Ramadge PJ, Haxby JV.

938   Function-based intersubject alignment of human cortical anatomy. Cerebral Cortex.

939   2010;20:130-140.

940   24. Conroy BR, Singer BD, Haxby JV, Ramadge PR. MRI-Based inter-subject cortical

941   alignment using functional connectivity. In Y Bengio, D Schuurmans, J Lafferty, CKI

942   Williams, A Culotta (eds), Advances in Neural Information Processing Systems 22.

943   2009: pp 378-386.

944   25. Conroy BR, Singer BD, Guntupalli JS, Ramadge PR, Haxby JV. Inter-subject

945   alignment of human cortical anatomy using functional connectivity. Neuroimage.

946   2013;81:400-411.

947   26. Guntupalli JS, Wheeler KG, Gobbini MI. Disentangling the representation of

948   identity from head view along the human face processing pathway. Cerebral

949   Cortex. 2017;27:46-53.

950   27. Connolly AC, Sha L, Guntupalli JS, Oosterhof N, Halchenko YO, Nastase SA, et al.

951   How the Human Brain Represents Perceived Dangerousness or "Predacity" of

952   Animals. J Neurosci. 2016;36: 5373–5384.

953   28. Visconti di Oleggio Castello M, Halchenko YO, Guntupalli JS, Gors JD, Gobbini MI.

954   The neural representation of familiar and unfamiliar faces in the distributed system

955   for face perception. Scientific Reports. 2017;7:12237.

956   29. Heinzle J, Kahnt T, Haynes J-D. Topographically specific functional connectivity

957   between visual field maps in the human brain. NeuroImage. 2011;56: 1426–1436.

958   30. Jbabdi S, Sotiropoulos SN, Behrens TE. The topographic connectome. Current

959   Opinion in Neurobiology. 2013;23: 207–215.

960   31. Haak KV, Marquand AF, Beckmann CF. Connectopic mapping with resting-state

961   fMRI. Neuroimage. 2017;epub ahead of print.

962   32. Langs G, Sweet A, Lashkari D, Tie Y, Rigolo L, Golby AJ, Golland P. Decoupling

963   function and anatomy in atlases of functional connectivity patterns: Language

964   mapping in tumor patients. Neuroimage. 2014;103:462-475.

965   33. Langs G, Wang D, Golland P, Mueller S, Pan R, Sabuncu MR, Sun W, Li K, Liu H.

966   Identifying shared networks in individuals by decoupling functional and anatomical

967   variability. Cerebral Cortex. 2016;26:4004-4014.

968   34. Beckmann CF, Mackay CE, Filippini N, Smith SM. Group comparison of

969   resting-state FMRI data using multi-subject ICA and dual regression. Organization of

970   Human Brain Mapping Abstracts. 2009.

971   35. Filippini N, MacIntosh BJ, Hough MG, Goodwin GM, Frisoni GB, Smith SM, et al.

972   Distinct patterns of brain activity in young carriers of the APOE-e4 allele.

973   Proceedings of the National Academy of Sciences, USA. 2009;106:7209-7214.

974   36. Yacoub E, Harel N, Uğurbil K. High-field fMRI unveils orientation columns in

975   humans. PNAS. 2008;105:10607–10612.

976   37. Nishimoto S, Vu AT, Naselaris T, Benjamini Y, Yu B, Gallant JL. Reconstructing Visual

977   Experiences from Brain Activity Evoked by Natural Movies. Current Biology.

978   2011;21: 1641–1646.

979   38. Kanwisher N. Functional specificity in the human brain: A window into the

980   functional architecture of the mind. PNAS. 2010;107: 11163–11170.

981   39. Freiwald WA, Tsao DY. Functional Compartmentalization and Viewpoint

982   Generalization Within the Macaque Face-Processing System. Science. 2010;330:

983   845–851.

984   40. Nastase SA, Connolly AC, Oosterhof NN, Halchenko YO, Guntupalli JS, Visconti di

985   Oleggio Castello M, Gors J, Gobbini MI, Haxby JV. Attention selectively reshapes

986   the geometry of distributed semantic representation. Cereb Cortex. 2017;27:

987   4277-4291.

988   41. DiCarlo JJ, Cox DD. Untangling invariant object recognition. Trends in Cognitive

989   Sciences. 2007;11: 333–341.

990   42. Cox RW. AFNI: software for analysis and visualization of functional magnetic

991   resonance neuroimages. Comput Biomed Res. 1996;29: 162–173.

992   43. Saad ZS, Reynolds RC, Argall B, Japee S, Cox RW. SUMA: an interface for

993   surface-based intra- and inter-subject analysis with AFNI. IEEE International

994   Symposium on Biomedical Imaging: Nano to Macro, 2004. 2004. Vol. 2; pp.

995   1510–1513.

996   44. Oosterhof NN, Wiestler T, Downing PE, Diedrichsen J. A comparison of

997   volume-based and surface-based multi-voxel pattern analysis. NeuroImage.

998   2011;56: 593–600

999   45. Hanke M, Halchenko YO, Sederberg PB, Hanson SJ, Haxby JV, Pollmann S.

1000   PyMVPA: A Python toolbox for multivariate pattern analysis of fMRI data.

1001   Neuroinformatics. 2009;7: 37–53.

1002   46. Schönemann PH. A generalized solution of the orthogonal procrustes problem.

1003   Psychometrika. 1966;31: 1–10.

1004   47. Gower JC. (1975). Generalized procrustes analysis. Psychometrika. 1975;40: 33–51.

1005   48. Chen P-H, Chen J, Yeshurun Y, Hasson U, Haxby JV, Ramadge PJ. A

1006   Reduced-dimension fMRI Shared Response Model. Proceedings of the 28th

1007   International Conference on Neural Information Processing Systems. Cambridge,

1008   MA, USA: MIT Press; 2015. pp. 460–468.

1009   49. Xu H, Lorbert A, Ramadge PJ, Guntupalli JS, Haxby JV. Regularized

1010   hyperalignment of multi-set fMRI data. 2012 IEEE Statistical Signal Processing

1011   Workshop (SSP). IEEE; 2012. pp. 229–232.

1012   50. Kriegeskorte N, Simmons WK, Bellgowan PSF, Baker CI. Circular analysis in systems

1013   neuroscience: the dangers of double dipping. Nat Neurosci. 2009;12: 535-540.

1014   51. Kirby KN, Gerlanc D. BootES: An R package for bootstrap confidence intervals on

1015   effect sizes. Behav Res. 2013;45: 905–927.

1016   52. Halchenko YO, Hanke M. Open is Not Enough. Let's Take the Next Step: An

1017   Integrated, Community-Driven Computing Platform for Neuroscience. Front

1018   Neuroinform. 2012;6.

1019   Supporting information legends

1020   S1 Text. Overview of supplemental data and figures on common model connectome

1021   based on responses to a movie.

1022   S2 Fig. Spatial granularity of shared connectivity profiles from the movie data. The

1023   common model connectome based on the movie data produced similar results to the

1024   common model connectome based on resting state data in terms of ISC of connectivity

1025   profiles (Fig 5) and the spatial granularity, as indexed by the PSF of ISCs. (A) Mean PSF

1026   slopes in functional ROIs. (B) Mean PSF across all ROIs.

1027   S3 Fig. ISC of representational geometries in the responses to movie time-points.

1028   Analysis procedure was identical to Fig 4 with results after RHA included for

1029   comparison. (A) ISC of representational geometry in each voxel mapped onto cortical

1030   surfaces after anatomical alignment, RHA, and CHA. (B) ISC of representational

1031   geometries in 24 functional ROIs and their mean after anatomical alignment and in the

1032   common model connectome. Bootstrapped testing showed significantly higher ISCs of

1033   representational geometry after both CHA and RHA relative to anatomical alignment in

1034   all ROIs, and some differences after CHA and RHA ("-" : CHA<RHA; "ns" : no

1035   significant difference between ISCs after CHA and RHA; "+" : CHA>RHA). CHA

1036   increased the ISC of representational geometry in all of the ROIs (ROI mean ISC=0.291)

1037   relative to anatomical alignment (ISC=0.173) (difference=0.118 [0.103, 0.129]), but the

1038   increase is slightly, but significantly, less than that provided by RHA (ISC=0.306)
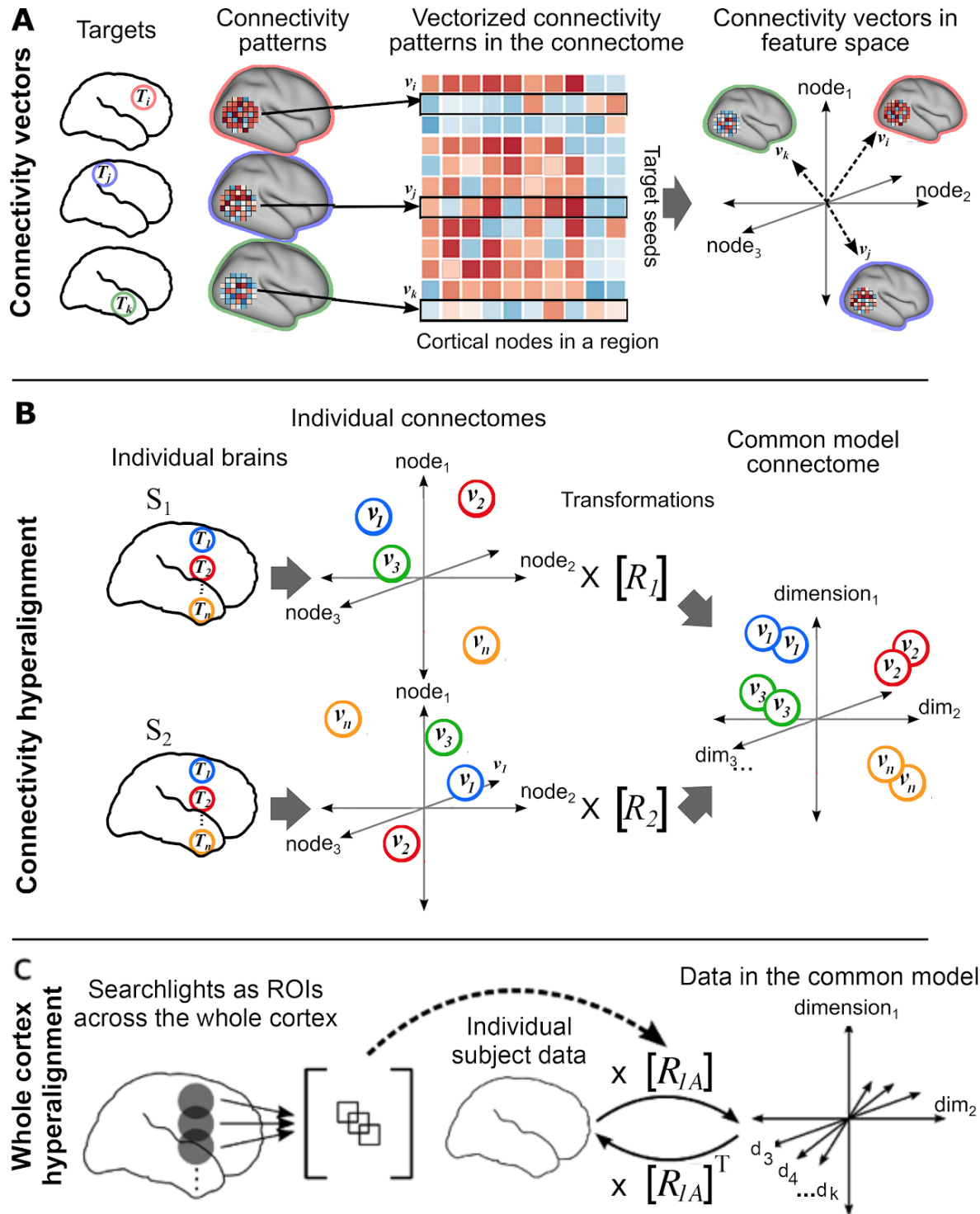
1039   (difference=0.015 [0.009, 0.019]).

1040   S4 Fig. Between-subject classification of movie segments. Analysis procedure was

1041   identical to Fig 4 with results after RHA included for comparison. (A) Classification

1042   accuracies in each searchlight mapped on cortical surfaces after anatomical alignment,

1043   RHA, and CHA. (B) Classification accuracies in 24 ROIs covering visual, auditory,

1044   cognitive, and social systems across the cortex and their mean after anatomical
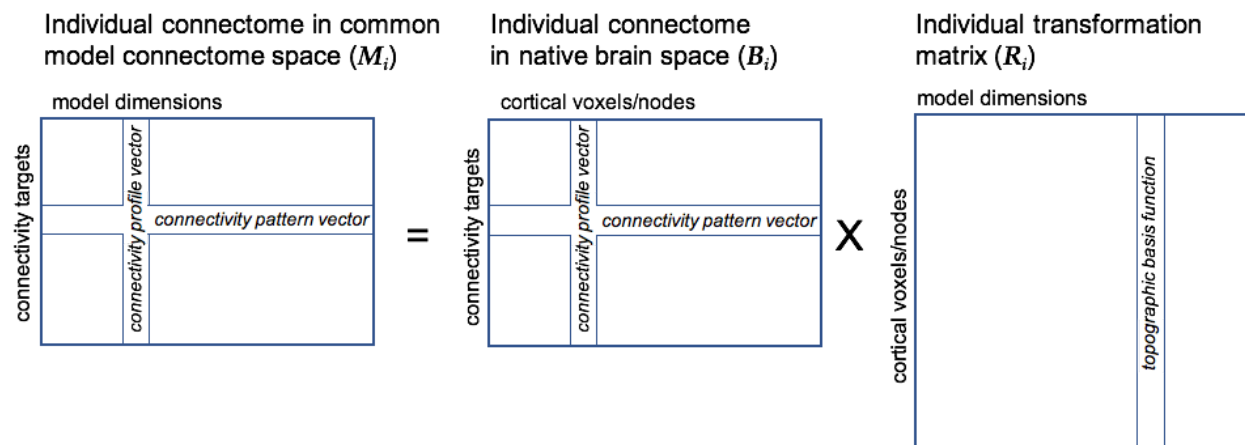
1045   alignment, RHA, and CHA. Bootstrapped testing showed significant, six to seven-fold

1046   higher accuracies after both the hyperalignment methods relative to anatomical

1047   alignment (ROI mean bsMVPC is 1.74%, 12.95%, 9.93% after anatomical alignment,

1048   RHA, and CHA, respectively and slightly but significantly higher accuracies after RHA

1049   relative to CHA (mean difference = 3.02% [2.52%, 3.40%]). (C) Classification accuracies

1050   using information from multiple systems across the whole cortex. Dimensionality of the

1051   data is reduced using SVD and classification is performed with different set sizes of top

1052   singular vectors. Peak accuracy is reached after 200 dimensions for hyperaligned data

1053   and at 50 dimensions for anatomically aligned data. Peak accuracy after RHA is 92.98%

1054   and after CHA is 89.61% (mean difference = 3.37% [2.32%, 4.99%]).

1055   S5 Fig. ISC of HCP task activation and contrast maps. Connectivity hyperalignment

1056   parameters derived from a session of resting state data were applied to the task maps

1057   and the correlation of these maps is computed between each subject and the average

1058   of others before and after hyperalignment. Hyperalignment improved correlations on

1059   average across all tasks and in all but two (Face-Shapes and Body-Average, labeled ns)

1060   individual task maps. The average correlation across task maps increased from 0.58 to

1061   0.65 (mean difference = 0.07 [0.06, 0.08]).

1062   S6 Table. Selected cortical loci implicated in visual, auditory, cognitive, and social
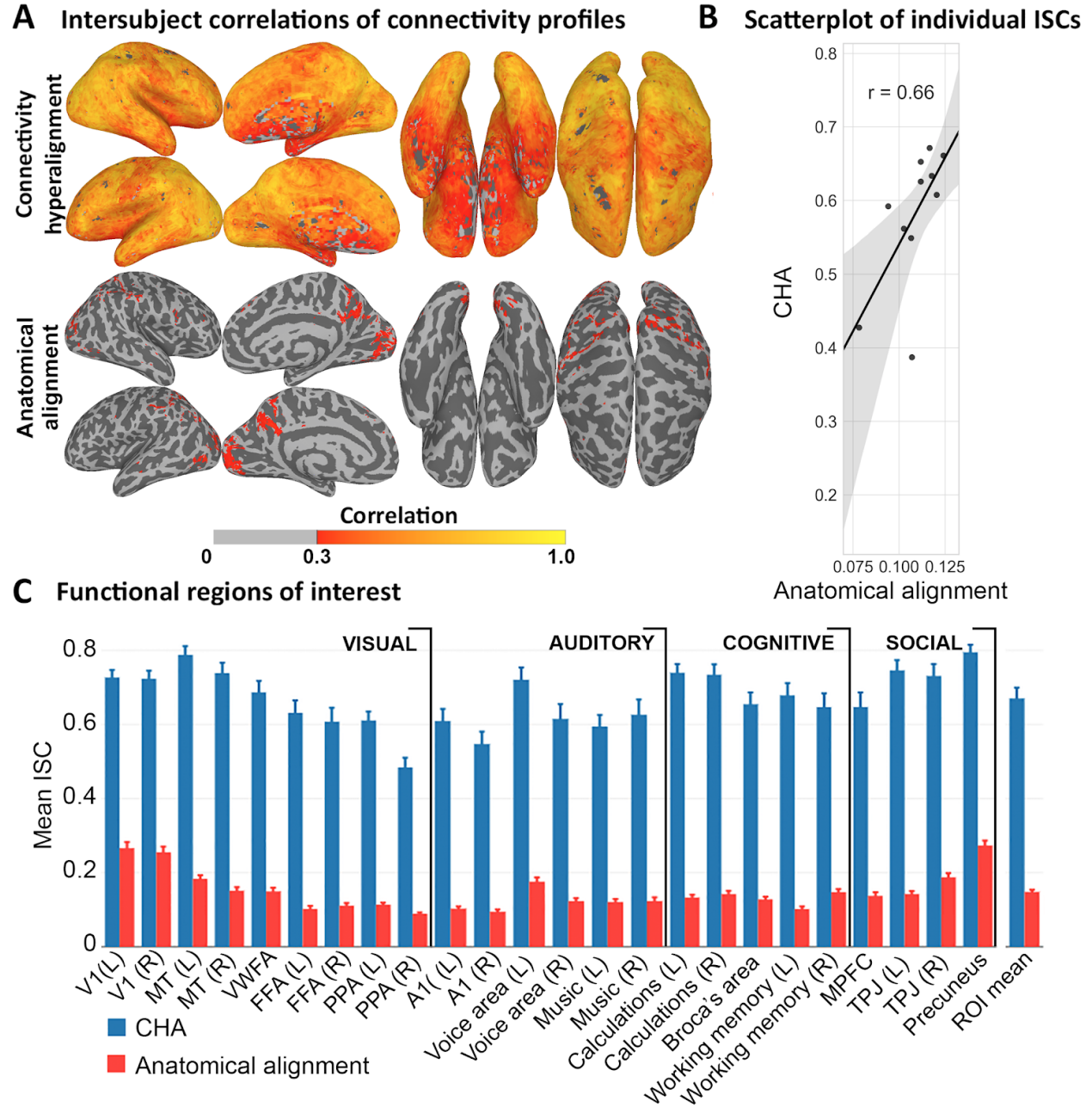
1063   functions from Neurosynth.

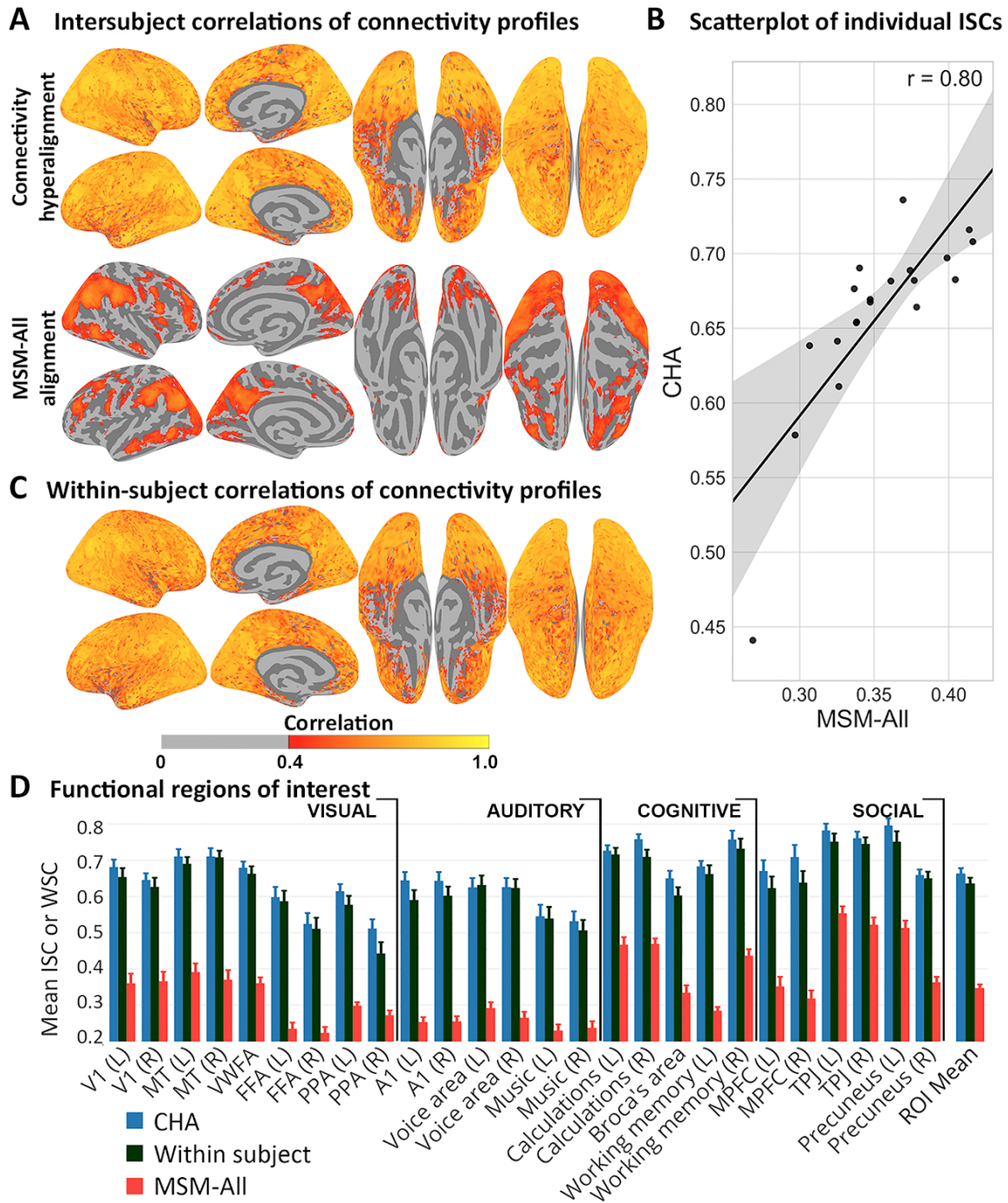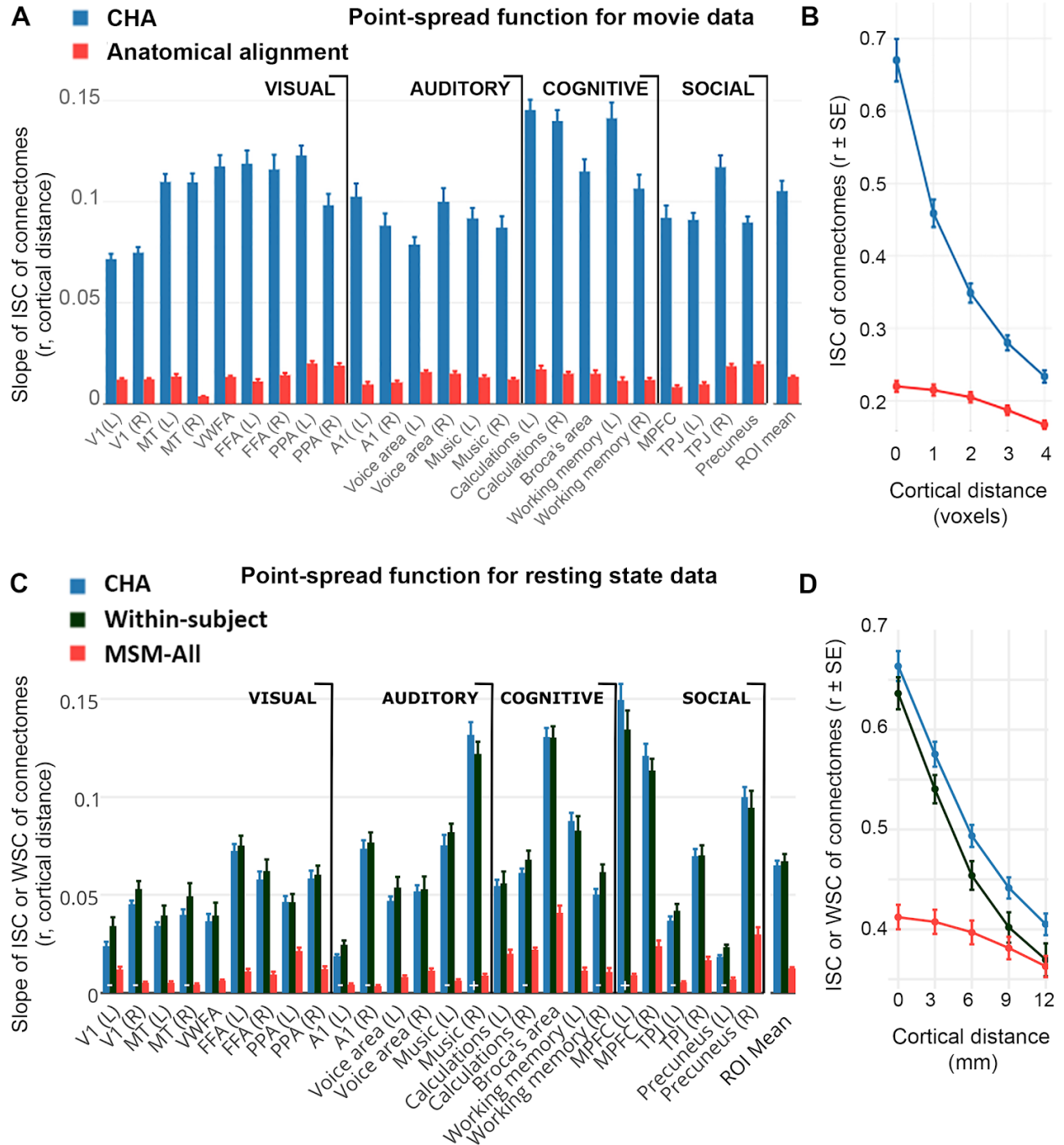1064   S7 Table. Task maps used from the HCP data.

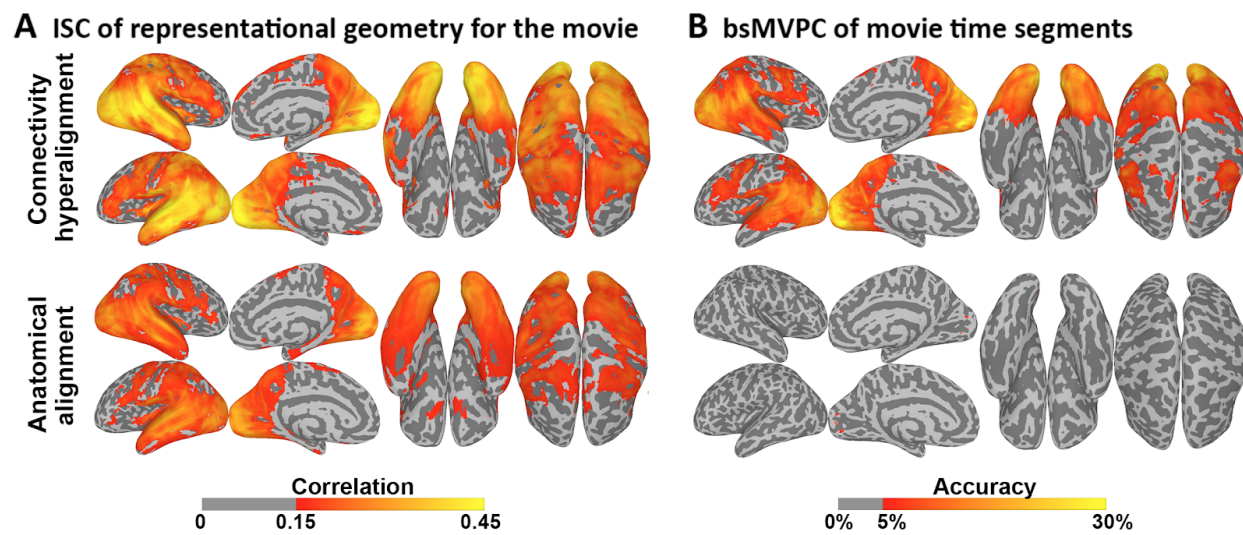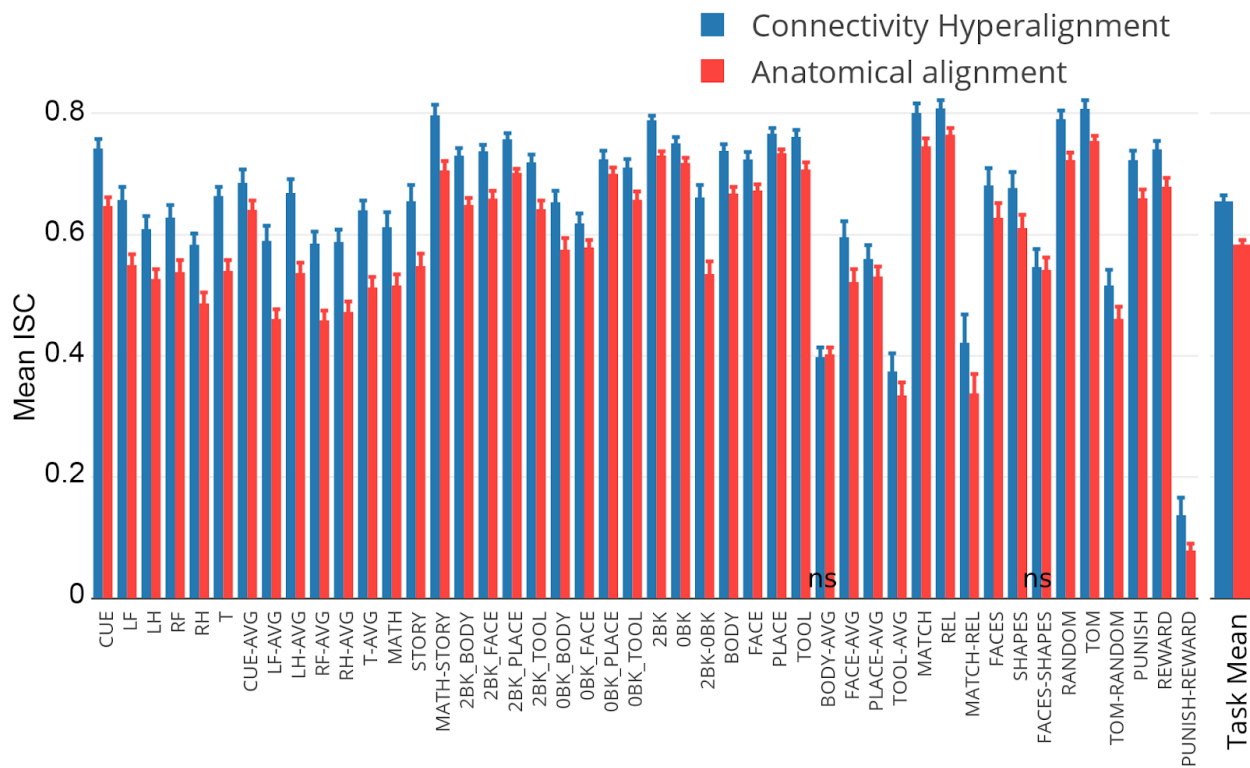Figure 1

Figure 2

Figure 3

Figure 4

Figure 5

A ISC of representational geometry for the movie

B bsMVPC of movie time segments

Figure 6

Figure 7

Figure 8